ARTICLE   OPEN

Check for updates

Charge dynamics of a noncentrosymmetric magnetic Weyl semimetal

R. Yang[1,10,11], M. Corasaniti [1,11], C. C. Le[2,3], C. Yue[4], Z. Hu[5,6], J. P. Hu [7,8,9], C. Petrovic [5,6] and L. Degiorgi [1✉]

The interplay of topology with magnetism in Weyl semimetals recently arose to a vanguard topic, because of novel physical scenarios with anomalous transport properties. Here, we address the charge dynamics of the noncentrosymmetric and ferromagnetic ($T_C \sim 15$ K) PrAlGe material and discover that it harbours electronic correlations, which are reflected in a sizeable reduction of the Fermi velocity with respect to the bare band value at low temperatures (T). At $T < T_C$, the optical response registers a band reconstruction, which additionally causes a reshuffling of spectral weight, pertinent to the electronic environment of the type-I Weyl fermions and tracing the remarkable anomalous Hall conductivity (AHC). With the support of first-principles calculations, we provide evidence for the intimate relationship between a topological resonance of the absorption spectrum and the progressively enhanced occupation of non-trivial states with large Berry curvatures, a requirement for AHC.

INTRODUCTION

The past decade has vividly witnessed fundamental discoveries of relativistic phenomena in a large variety of novel solid-state topological materials[1–3]. Astonishing physical properties are anticipated in the Weyl semimetals, for which their topology derives from the split of the doubly degenerate, massless Dirac fermions because of broken time-reversal (TR) or space-inversion (SI) symmetry or even a combination of both[4–6].

Lately, the research focus moves to the crucial link between magnetism and topology[7]. Early evidence for magnetic Weyl semimetals encounters for instance the non-collinear antiferromagnet Mn_3Sn[8] and the Kagomé ferromagnetic (FM) $Co_3Sn_2S_2$[9], both being centrosymmetric. The noncentrosymmetric RAlGe compounds (R = rare earth) recently advance as a new family of magnetic materials paving the way to intriguing quantum states and hosting emergent topological properties of Weyl fermions[10]. Of particular interest is PrAlGe (with Pr $4f^2$ orbitals), which exhibits a FM order below $T_C \sim 15$ K arising from the coupling between the f-electrons local moments[10–14]. The latter serve as an effective Zeeman field, making the conduction bands (s, p and d orbitals) spin-polarised[10]. The resulting broken TR symmetry displaces the Weyl nodes in the reciprocal space, therefore ensuring, together with the energy displacement due to the broken SI symmetry, the lift of the degeneracy at the original Dirac states. Angle-resolved-photoemission-spectroscopy (ARPES) experiments reveal the topological semimetallic nature of PrAlGe and highlight the linear energy-dispersion at its Weyl nodes[11]. The alliance between topology and magnetism renders PrAlGe even a suitable candidate for fundamental studies in view of innovative applications, as when designing spintronic devices[15,16].

The prediction from first-principles calculations[10] that the Weyl fermions in PrAlGe are in proximity of the Fermi level (E_F) and its established large anomalous Hall conductivity (AHC) below T_C[11,12]

have a significant implication: the enhanced Berry curvature fields associated with those Weyl nodes and concomitant with the broken TR symmetry may deem necessary to generate a large, intrinsic (topological) anomalous Hall effect[17]. PrAlGe is thus an ideal playground in order to chase the elusive ingredients framing the relationship between topology and peculiar transport properties.

By exploring the temperature (T) dependence of the real part ($\sigma_1(\omega)$) of the optical conductivity[18], achieved over an extremely broad spectral range and combined with a dedicated first-principles calculation, we ultimately capture the spectroscopic hallmark of the intrinsic anomalous Hall effect in PrAlGe. Henceforth, this is of significance even from a methodological point of view, since our mode of operation may represent a straightforward, broadband yet alternative approach to magneto-optical methods[19–23], when keeping track of the impact of the electronic band structure on the anomalous transport properties across a magnetic transition.

RESULTS

Optical conductivity

We commence our data survey with Fig. 1, which displays the T dependence of $\sigma_1(\omega)$ below 3000 cm^{-1}. Its inset compares the spectra at 5 and 300 K over the whole measured spectral range. We refer to Methods and to the Supplementary Note 3 for more details. Upon increasing the frequency from zero, we first observe the metallic-like (Drude) zero-energy mode, followed by a rather broad absorption at far-infrared (FIR) energy scales. These features undergo the most prominent T dependence: both narrow with decreasing T and upon crossing the FM transition the high frequency shoulder of the FIR absorption gets suppressed, mainly leading to a cusp-like feature (peaked at about 500 cm^{-1}) and to

^{1}Laboratorium für Festkörperphysik, ETH - Zürich, 8093 Zürich, Switzerland. ^{2}Max Planck Institute for Chemical Physics of Solids, 01187 Dresden, Germany. ^{3}RIKEN Interdisciplinary Theoretical and Mathematical Sciences (iTHEMS), Wako, Saitama 351-0198, Japan. ^{4}Department of Physics, University of Fribourg, 1700 Fribourg, Switzerland. ^{5}Condensed Matter Physics and Materials Science Department, Brookhaven National Laboratory, Upton, NY 11973, USA. ^{6}Department of Materials Science and Chemical Engineering, Stony Brook University, Stony Brook, NY 11790, USA. ^{7}Beijing National Laboratory for Condensed Matter Physics, Institute of Physics, Chinese Academy of Sciences, 100190 Beijing, China. ^{8}Kavli Institute for Theoretical Sciences and CAS Center for Excellence in Topological Quantum Computation, University of Chinese Academy of Sciences, 100190 Beijing, China. ^{9}South Bay Interdisciplinary Science Center, Dongguan, Guangdong Province, China. ^{10}Present address: Physikalisches Institut, Universität Stuttgart, Pfaffenwaldring 57, 70569 Stuttgart, Germany. ^{11}These authors contributed equally: R. Yang, M. Corasaniti. ✉email: degiorgi@solid.phys.ethz.ch
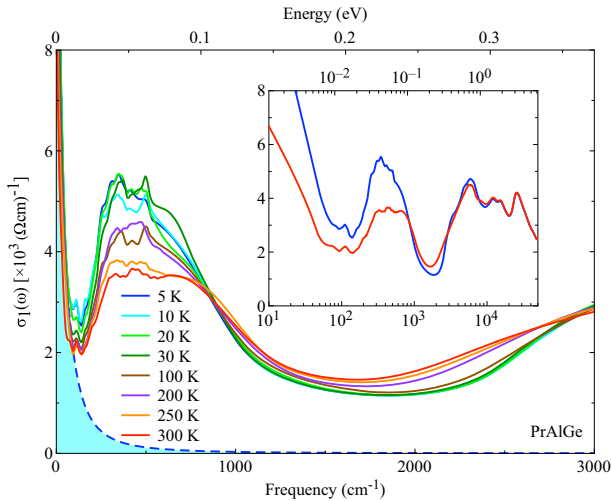
Fig. 1 Optical conductivity of PrAlGe. T dependence of $\sigma_1(\omega)$ of PrAlGe below 3000 cm^{-1} (1 eV $= 8.06548 \times 10^3$ cm^{-1}). The thick blue dashed line accentuates the intraband $\sigma_1^{Drude}(\omega)$ component at 5 K, obtained within the two-Drude approach (i.e., sum of the narrow (D1) and broad (D2) Drude terms, Supplementary Note 4, Supplementary Equation 1 and Supplementary Fig. 3). The same procedure was applied at all T. The inset shows $\sigma_1(\omega)$ in the total measured energy interval at 300 and 5 K (please note the logarithmic energy scale).
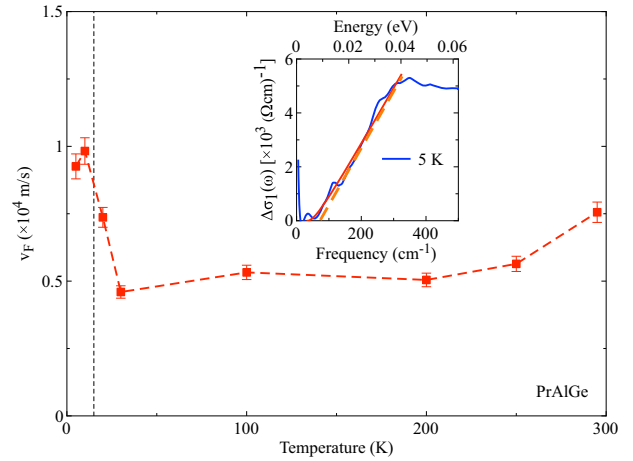

Fig. 2 Fermi velocity in PrAlGe. T dependence of v_F, extracted from $\Delta\sigma_1(\omega) \sim \omega/v_F$ (see text). The vertical dashed line marks $T_C \sim 15$ K[12]. The error bars estimation is provided at Supplementary Note 5. The inset displays the interband contribution $\Delta\sigma_1(\omega) = \sigma_1(\omega) - \sigma_1^{Drude}(\omega)$ at 5 K ($\sigma_1^{Drude}(\omega)$ is shown in Fig. 1). The red line is the fit of $\Delta\sigma_1(\omega)$ after Supplementary Equation 2, which merges into a linear frequency dependence (thick orange dashed line) at $\omega > 2\Delta$.

an accumulation of spectral weight (SW) (i.e., SW $\sim \int\sigma_1(\omega)d\omega$, see Supplementary Note 4) at FIR energies. We will later argue that this adumbrated SW redistribution across T_C is remarkably univocal, when compared to the situation in the non-magnetic LaAlGe. A smooth SW removal with decreasing T is then observed in the mid-infrared energy interval (i.e., 1500–3000 cm^{-1}), with accompanying SW redistribution at higher energies, up to the near-infrared spectral range (i.e., 4000–10,000 cm^{-1}, inset of Fig. 1). The $\sigma_1(\omega)$ spectra at all T finally merge at ultra-violet energies (inset of Fig. 1) into the T-independent absorptions, which are almost identical in all RAlGe compounds[24].

In analogy to the analysis of the charge dynamics recently reported for LaAlGe and CeAlGe[24], the zero-energy mode in $\sigma_1(\omega)$ (i.e., the intraband component, $\sigma_1^{Drude}(\omega)$, thick blue dashed line in Fig. 1) of PrAlGe is well accounted for by two Drude terms (Supplementary Note 4, Supplementary Equation 1 and Supplementary Fig. 3). By subtracting $\sigma_1^{Drude}(\omega)$ from $\sigma_1(\omega)$ at each T, we can better emphasise its interband contribution (i.e., $\Delta\sigma_1(\omega) = \sigma_1(\omega) - \sigma_1^{Drude}(\omega)$), shown in the inset of Fig. 2 at 5 K for the FIR energy scales. The resulting $\Delta\sigma_1(\omega)$ comprises a characteristic (single) linear frequency dependence at its low energy tail, which is distinct from the kink feature observed in $\Delta\sigma_1(\omega)$ of LaAlGe and CeAlGe[24] and is definitely reminiscent of the typical optical response for type-I Weyl semimetals[25]. The linear frequency dependence of $\sigma_1(\omega)$ is the direct consequence of the linear dispersion relation at the Dirac cones, from which Weyl states originate[26]. That the Weyl cones located near E_F are not tilted (as it is the case for type-II) is also consistent with both theoretical predictions and experimental observations; after ref. [10], one may expect about 32 type-I Weyl nodes and about 8 type-II Weyl ones at energies below 50 meV, even though the latter are not observed in ARPES data[11]. Moreover, we remark the intercept at finite frequency of the (extrapolated) linear frequency dependence in $\Delta\sigma_1(\omega)$ (thick orange dashed line in the inset of Fig. 2), which indicates a tiny gap ($2\Delta \sim 2$–6 meV) at the Dirac/Weyl nodes, similar to graphene[26,27], ZrTe$_5$[28] and Co$_3$Sn$_2$S$_2$[29,30]. It could be here generated for instance by the reinforced virtue of the spin-orbit coupling (SOC) particularly below T_C[31] or as a consequence of electronic correlations[32].

Fermi velocity

We can exploit the steep linear frequency dependence of $\Delta\sigma_1(\omega)$ in order to extract the Fermi velocity (v_F). Since the non-trivial bands mostly shape the electronic band structure close to E_F[10,11], we are confident that a superposition of trivial interband transitions[33] is not relevant in PrAlGe and therefore will not invalidate our following analysis. In fact, after Supplementary Equation 2 we can state that the slope of $\Delta\sigma_1(\omega)$ at $\omega > 2\Delta$ is given by $\frac{NG_0}{24v_F}$[25–28,34] (Supplementary Note 5), with G_0 being the quantum conductance and $N = 32$ and 16 the number of type-I (W3 and W4) Weyl points seating close to E_F below and above T_C, respectively[10]. The extracted T-dependent v_F is then shown in Fig. 2.

With decreasing $T > T_C$, v_F tends to be suppressed, similar to the Weyl semimetal YbMnBi$_2$[35], yet in a less pronounced fashion than in CeAlGe below 100 K[24]. The low T values of v_F in PrAlGe are overall smaller than those in typical weakly interacting Weyl semimetals[36,37]. Moreover, the T dependence of v_F is here opposite to the findings in LaAlGe (without f-electrons), showing a continuous increase, compatible with the T dependence of a two and three dimensional Dirac material within the Hartree–Fock approximation (i.e., $v_F \sim \ln(1/T)$)[24,38]. Such a logarithmic divergence of $v_F(T)$ is supposed to vanish if correlation effects are taken into account[39–42]. Therefore, we advance that the rather flat $v_F(T)$ in quite the entire T range above T_C and its still suppressed values at low T with respect to the non-correlated LaAlGe material (i.e., with $v_F = 3.2 \times 10^4$ m/s at 5 K[24]) could hint at the major impact of correlation effects, similar to earlier observations in YbPtBi[42] and CeAlGe[24] as well as in nodal-line Dirac semimetals[43]. The renormalisation of v_F in PrAlGe, compared to the bare band value supplied by LaAlGe[24], also pairs with the strongly reduced kinetic energy estimated from the Drude SW at low T (see details in Supplementary Note 4), another well-established signature of electronic correlations[29,44,45]. Conversely, the suppressed scattering from magnetic fluctuations in the FM state, as suggested by the drop of the resistivity (Supplementary Fig. 1), causes a renewed, moderate increase of v_F across T_C (Fig. 2).

Spectral weight and AHC

Before going any further with the data interpretation, we highlight that $\Delta\sigma_1(\omega)$ can be phenomenologically described by a
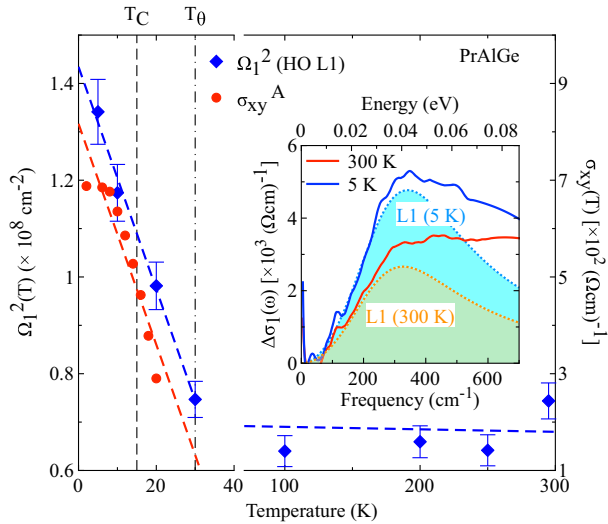
Fig. 3 Spectral weight versus AHC in PrAlGe. T dependence of the squared strength (Ω_1^2) of HO L1 (Supplementary Equation 1 and Supplementary Fig. 3) and of the Hall conductivity σ_{xy}, reproduced from ref. [12]. σ_{xy} is read at the magnetic field $H = 6\,T$ ($\mathbf{H}\|c$-axis), where it saturates. It is known that $\sigma_{xy} \sim \sigma_{xy}^A$ [12]. The linear fits (dashed lines) are guide to the eyes. The vertical dashed and dashed-dotted lines mark T_C and T_Θ [12], respectively. The error bars of Ω_1^2 are estimated numerically within the non-linear least-squares fit technique. Inset: $\Delta\sigma_1(\omega)$ at 5 and 300 K with HO L1, showing its enhanced SW (colour shaded area) at $T < T_C$ (see also Supplementary Note 4 and Supplementary Fig. 6).

combination of Lorentz (L) harmonic oscillators (HOs in Supplementary Equation 1 and Supplementary Fig. 3), which also help on elucidating the SW redistribution beyond the itinerant components of the charge dynamics. The SW of each HO corresponds to the square of its strength (Ω_j) (Supplementary Note 4 and Supplementary Equation 1). We follow the same fit procedure successfully applied for the La and Ce compositions[24], which then guarantees a consistent data elaboration and a robust analysis of the T dependence of $\sigma_1(\omega)$ across T_C, as evinced in Fig. 1. Herewith, we bring out HOs L1 and L2 (Supplementary Fig. 3), which devise the minimal approach of $\Delta\sigma_1(\omega)$ below 0.1 eV and experience a SW reshuffling. In particular at this point, we underscore that HO L1, which forges the low frequency edge of the FIR and Weyl states related absorption in $\Delta\sigma_1(\omega)$, is prone to considerably gain SW $\sim \Omega_1^2$ at low T (inset of Fig. 3 and for more insights see discussion of Supplementary Fig. 6 in Supplementary Note 4). Interestingly enough, the sudden increase of Ω_1^2 starts at the Curie–Weiss temperature $T_\Theta \sim 30\,K$ [12], below which the intrinsic AHC (i.e., σ_{xy}^A) is already different from zero (Fig. 3). We speculate that this might signal the relevance of magnetic fluctuations[46] for both optical response and transport properties at $T_C < T < T_\Theta$. The enhancement of SW for HO L1 going hand in hand with the onset of the large σ_{xy}^A in PrAlGe at $T \lesssim 30\,K$ is not detected in the paramagnetic (PM) LaAlGe (Supplementary Note 4) and is our salient finding. It may allude to the association of the topological resonance with states of intense Berry curvature[22,23], upon which we are going to argue for the rest of this paper.

DISCUSSION

The first-principles calculation of the electronic band structure is very instrumental, in order to address the origin and consequences of the absorption features in $\sigma_1(\omega)$, particularly at the energy scales involving the Weyl states. As detailed in

Supplementary Fig. 7, the electronic band structure, achieved in the PM and FM state upon including SOC, agrees with similar investigations[10,47] and is broadly confirmed by ARPES[11]. In the energy interval of about 100 meV around E_F, the non-trivial bands have been postulated to accommodate large Berry curvatures[10,11], so that changes of their occupation across T_C is supposed to determine the magnitude of AHC. Therefore, we primarily look at regions in the Brillouin zone (BZ), where Weyl nodes group together (Fig. 4a, b) and Fermi surface pockets mainly exist[47], and consider those cuts in the reciprocal space (i.e., off the high-symmetry directions) with k-paths running nearby representative Weyl nodes (black stars PM1/2 and FM1/2/3 in Fig. 4a, b and Supplementary Table I)[10,11]. Figure 4c–g then emphasise the evolution of the resulting band structure between the PM and FM state (for details see Supplementary Note 6). The overall band structure calculation sets the stage in order to achieve a reliable estimation of the interband part of $\sigma_1(\omega)$ (i.e., $\Delta\sigma_1(\omega)$) within the Kubo–Greenwood formula (Supplementary Equation 3), which is displayed in Fig. 4h and can be mapped onto its experimental counterpart (Fig. 1 and inset of Figs. 2 and 3). Two features at ~250 and 500 cm^{-1} (green and red arrows in Fig. 4h) catch our attention in the calculated $\Delta\sigma_1(\omega)$ of the PM state, since they occur at energies very close to the dominant FIR absorption in the experimental $\Delta\sigma_1(\omega)$. By inspecting the electronic band structure, we actually learn that these absorptions may correspond to direct interband transitions (green and red bars in Fig. 4c, d and Supplementary Fig. 8) at k-points in BZ meshing the Weyl nodes[10]. Into the FM state, the electronic band reconstruction, because of the effects due to the Zeeman splitting, leads to a differentiation of the states occupation near E_F and to a new distribution of direct interband transitions (blue bars in Fig. 4e–g). This merges into a broad convolution of absorptions in $\Delta\sigma_1(\omega)$, which strengthen and induce a SW redistribution within the energy interval 130–400 cm^{-1} (Fig. 4h) below T_C. The theoretical $\Delta\sigma_1(\omega)$ (Fig. 4h) fairly copies with the main trend of the experimental quantity at least below 1000 cm^{-1} (Fig. 1 and inset of Fig. 3). In Supplementary Note 7, we deal with the deviations encountered above 0.1 eV between the experimental and calculated $\sigma_1(\omega)$.

The reconstruction of the electronic band structure across T_C then triggers the evolution of the (integrated) Berry curvature (see Supplementary Note 8), so that, as exemplified by Fig. 4i, there is an imbalance between its negative and positive values[47]. This effectively happens at k-points in BZ situated in proximity to the Weyl nodes, like those (black stars in Fig. 4a, b, i) at which the pronounced FIR interband transitions are taking place, in accordance with Fig. 4h. The just mentioned imbalance is a direct corollary of the broken TR symmetry in the FM state, as a consequence of which relevant parts of the electronic band structure get asymmetric (i.e., between $-k$ and $+k$ directions) below T_C (Fig. 4e–g) than above T_C (Fig. 4c, d). In conjunction with these arguments, we offer a complementary discussion at Supplementary Notes 4 and 8 and with Supplementary Fig. 9. In the end, this conspires in promoting the enhancement of σ_{xy}^A [11,12,47]. Since σ_{xy}^A is proportional to the BZ integral of the convolution of the Berry curvature with the T dependent occupation function[48,49], Fig. 3 indeed conveys the connection between optics and σ_{xy}^A: the observed increasing strength (Ω_1) in HO L1 at $T < T_\Theta$ (Fig. 3) generally mimics the empowered matrix-element of the dipole-active interband transition (see Supplementary Note 4) at topologically driven band points upon entering the FM state[47] and equally indicates the increasing occupation of the significant states participating to the intrinsic AHC[22,23] (further details at Supplementary Note 6). Finally, the intimate relationship between σ_{xy}^A and the SW reshuffling (Fig. 3), pertinent to the excitations around the Weyl nodes and imprinting the Berry curvature, evidences a strong similarity with our previous findings in the van der Waals Fe_3GeTe_2 ferromagnet[50]. We conjecture that this seems to be a generic, common feature in
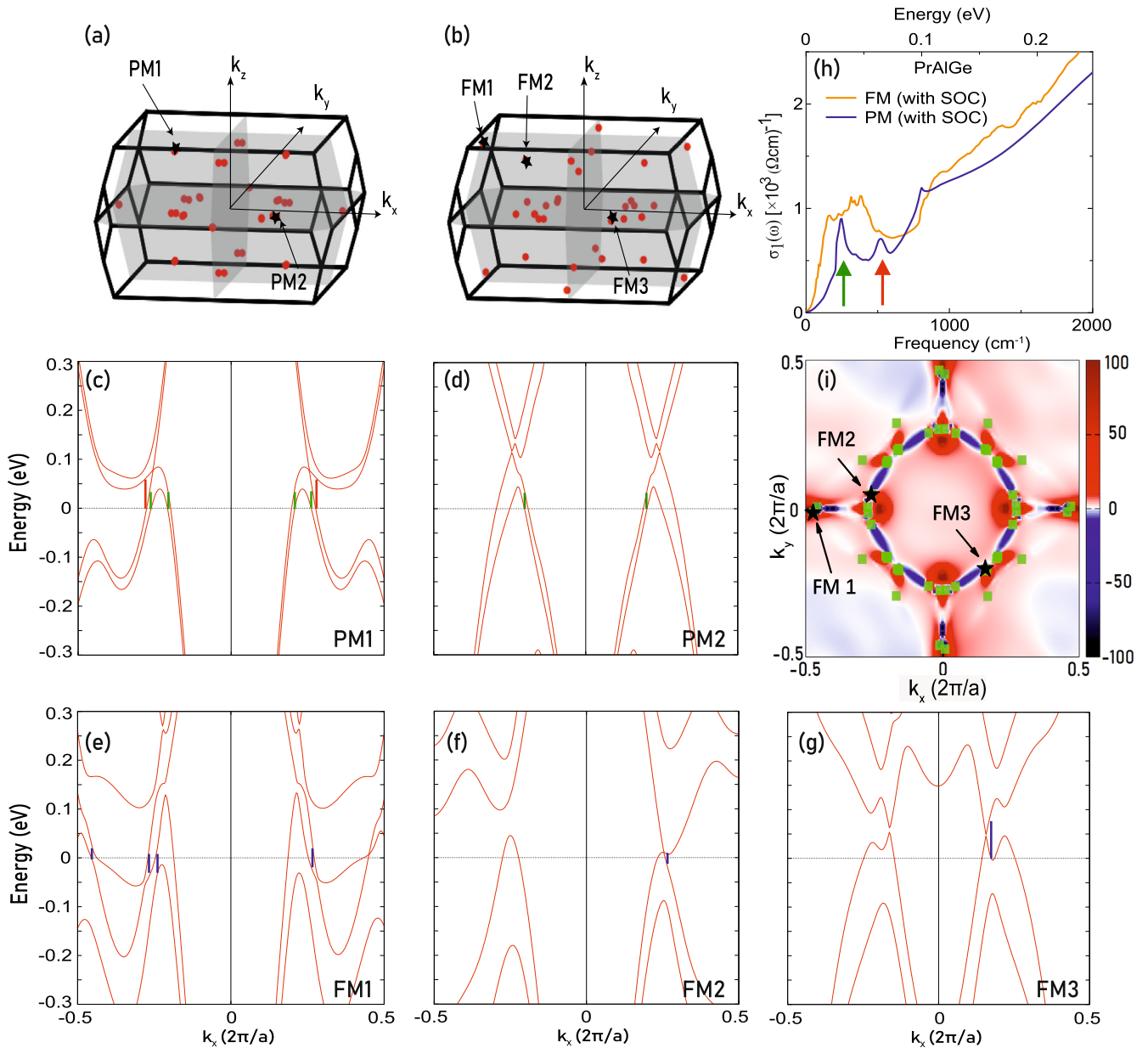
Fig. 4   First-principles calculations in PrAlGe. a, b Schemes of BZ indicating the locations of the Weyl nodes in the PM and FM state[10]. **c–g** First-principles calculation of the electronic band structure with SOC in the PM (**c, d**) as well as FM (**e–g**) state along k-paths in BZ, near some specific Weyl nodes (i.e., black stars PM1 and PM2 as well as FM1, FM2 and FM3 in **a, b** and **i** for the PM and FM state, respectively). The coloured bars in **c–g** point out a selection of representative interband transitions, then mapped onto $\Delta\sigma_1(\omega)$. The green and red bars refer to the transitions in the PM state, while the blue ones to those in the FM state. **h** Calculation of the interband part of $\sigma_1(\omega)$ (i.e., $\Delta\sigma_1(\omega)$) in both the PM and FM state, derived from the electronic band structure (Supplementary Equation 3). The colour code for the arrows matches the one of the bars in **c, d**, thus establishing their relationship. **i** Effective Berry curvature (i.e., its difference between the PM and FM state, Supplementary Fig. 9) integrated along k_z as a function of k_x and k_y from our ab initio calculations, which emphasises its strong enhancement in the FM state at those k-points of BZ almost coincident with the (projected) Weyl nodes (green symbols). Black stars foreground the selected Weyl nodes in the FM state, as in **b**. We refer to Supplementary Notes 6, 7 and 8 for details about all calculations.

materials displaying large AHC, even benefiting from electronic correlations at low T[42,51].

In conclusion, measurements of the charge dynamics of the noncentrosymmetric, topological correlated PrAlGe prove themselves to be a superior approach in order to satisfy the quest for the spectroscopic link between the reconstructed electronic band structure across the FM transition and the onset of the large AHC. The presence of the non-trivial Weyl states near E_F with large Berry curvature turns out to be decisive, when making an impact in the anomalous transport properties of the title material. At last, we

may also envisage our robust experiment as future best practice with additional tunable variables, like pressure and magnetic field.

METHODS

Sample preparation

The single crystals of PrAlGe were grown by the high temperature self-flux method[52]. Further details about the sample preparation can be found at Supplementary Note 1.

Optical experiment

The optical reflectivity $R(\omega)$ as a function of temperature was first measured from the far-infrared up to the ultra-violet (i.e., ~30–5×10^4 cm^{-1}). The real part $\sigma_1(\omega)$ of the optical conductivity was then obtained via the Kramers–Kronig transformation of $R(\omega)$ by applying suitable extrapolations at low and high frequencies[18]. Further details about this experiment can be found at Supplementary Note 3.

First-principles calculations

Calculations of the electronic band structure were performed using density functional theory as implemented in the Vienna ab initio simulation package code[53–55]. Further details about the band structure calculations can be found at Supplementary Note 6.

DATA AVAILABILITY

The data that support the findings of this study are available from the corresponding author upon reasonable request.

REFERENCES

1. Hasan, M. Z. & Kane, C. L. Colloquium: Topological insulators. *Rev. Mod. Phys.* **82**, 3045–3067 (2010).
2. Armitage, N. P., Mele, E. J. & Vishwanath, A. Weyl and Dirac semimetals in three-dimensional solids. *Rev. Mod. Phys.* **90**, 015001 (2018).
3. Lv, B. Q., Qian, T. & Ding, H. Experimental perspective on three-dimensional topological semimetals. *Rev. Mod. Phys.* **93**, 025002 (2021).
4. Weyl, H. Elektron und Gravitation. I. *Z. Phys.* **56**, 330–352 (1929).
5. Burkov, A. A., Hook, M. D. & Balents, L. Topological nodal semimetals. *Phys. Rev. B* **84**, 235126 (2011).
6. Nagaosa, N., Morimoto, T. & Tokura, Y. Transport, magnetic and optical properties of Weyl materials. *Nat. Rev. Mater.* **5**, 621–636 (2020).
7. Bernevig, B. A., Felser, C. & Beidenkopf, H. Progress and prospects in magnetic topological materials. *Nature* **603**, 41–51 (2022).
8. Kuroda, K. et al. Evidence for magnetic Weyl fermions in a correlated metal. *Nat. Mater.* **16**, 1090–1095 (2017).
9. Liu, D. F. et al. Magnetic Weyl semimetal phase in a Kagomé crystal. *Science* **365**, 1282–1285 (2019).
10. Chang, G. et al. Magnetic and noncentrosymmetric Weyl fermion semimetals in the *R*AlGe family of compounds (*R* = rare − earth). *Phys. Rev. B* **97**, 041104(R) (2018).
11. Sanchez, D. S. et al. Observation of Weyl fermions in a magnetic non-centrosymmetric crystal. *Nat. Commun.* **11**, 3356 (2020).
12. Meng, B. et al. Large anomalous Hall effect in ferromagnetic Weyl semimetal candidate PrAlGe. *APL Mater.* **7**, 051110 (2019).
13. Puphal, P. et al. Bulk single-crystal growth of the theoretically predicted magnetic Weyl semimetals *R*AlGe (*R* = Pr, Ce). *Phys. Rev. Mater.* **3**, 024204 (2019).
14. Liu, W. et al. Critical behavior of the magnetic Weyl semimetal PrAlGe. *Phys. Rev. B* **103**, 214401 (2021).
15. Liu, C.-X., Zhang, S.-C. & Qi, X.-L. The quantum anomalous Hall effect: theory and experiment. *Annu. Rev. Condens. Matter Phys.* **7**, 301–321 (2016).
16. Wang, J., Lian, B. & Zhang, S.-C. Generation of spin currents by magnetic field in *T*- and *P*-broken materials. *SPIN* **09**, 1940013 (2019).
17. Manna, K., Sun, Y., Muechler, L., Kübler, J. & Felser, C. Heusler, Weyl and Berry. *Nat. Rev. Mater.* **3**, 244–256 (2018).
18. Dressel, M. & Gruner, G. *Electrodynamics of Solids* (Cambridge University Press, 2002).
19. Fang, Z. et al. The anomalous Hall effect and magnetic monopoles in momentum space. *Science* **302**, 92–95 (2003).
20. Iguchi, S. et al. Optical probe for anomalous Hall resonance in ferromagnets with spin chirality. *Phys. Rev. Lett.* **103**, 267206 (2009).
21. Shimano, R. et al. Terahertz Faraday rotation induced by an anomalous Hall effect in the itinerant ferromagnet SrRuO₃. *EPL (Europhys. Lett.)* **95**, 17002 (2011).
22. Okamura, Y. et al. Giant magneto-optical responses in magnetic Weyl semimetal Co₃Sn₂S₂. *Nat. Commun.* **11**, 4619 (2020).
23. Kato, Y. D. et al. Optical anomalous Hall effect enhanced by flat bands in ferromagnetic van der Waals semimetal. *npj Quantum Mater.* **7**, 73 (2022).
24. Corasaniti, M. et al. Evidence for correlation effects in noncentrosymmetric type-II Weyl semimetals. *Phys. Rev. B* **104**, L121112 (2021).
25. Pronin, A. V. & Dressel, M. Nodal semimetals: a survey on optical conductivity. *Phys. Status Solidi (B)* **258**, 2000027 (2021). And references therein.
26. Tabert, C. J., Carbotte, J. P. & Nicol, E. J. Optical and transport properties in three-dimensional Dirac and Weyl semimetals. *Phys. Rev. B* **93**, 085426 (2016).
27. Benfatto, L. & Cappelluti, E. Spectroscopic signatures of massless gap opening in graphene. *Phys. Rev. B* **78**, 115434 (2008).
28. Xu, B. et al. Temperature-driven topological phase transition and intermediate Dirac semimetal phase in ZrTe₅. *Phys. Rev. Lett.* **121**, 187401 (2018).
29. Xu, Y. et al. Electronic correlations and flattened band in magnetic Weyl semimetal candidate Co₃Sn₂S₂. *Nat. Commun.* **11**, 3985 (2020).
30. Yang, R. et al. Magnetization-induced band shift in ferromagnetic Weyl semimetal Co₃Sn₂S₂. *Phys. Rev. Lett.* **124**, 077403 (2020).
31. Kim, K. et al. Large anomalous Hall current induced by topological nodal lines in a ferromagnetic van der Waals semimetal. *Nat. Mater.* **17**, 794–799 (2018).
32. Morimoto, T. & Nagaosa, N. Weyl Mott insulator. *Sci. Rep.* **6**, 19853 (2016).
33. Frenzel, A. J. et al. Anisotropic electrodynamics of type-II Weyl semimetal candidate WTe₂. *Phys. Rev. B* **95**, 245140 (2017).
34. Hosur, P., Parameswaran, S. A. & Vishwanath, A. Charge transport in Weyl semimetals. *Phys. Rev. Lett.* **108**, 046602 (2012).
35. Chinotti, M., Pal, A., Ren, W. J., Petrovic, C. & Degiorgi, L. Electrodynamic response of the type-II Weyl semimetal YbMnBi₂. *Phys. Rev. B* **94**, 245101 (2016).
36. Xu, S.-Y. et al. Experimental discovery of a topological Weyl semimetal state in TaP. *Sci. Adv.* https://advances.sciencemag.org/content/1/10/e1501092 (2015).
37. Lv, B. Q. et al. Experimental discovery of Weyl semimetal TaAs. *Phys. Rev. X* **5**, 031013 (2015).
38. Setiawan, F. & Das Sarma, S. Temperature-dependent many-body effects in Dirac-Weyl materials: Interacting compressibility and quasiparticle velocity. *Phys. Rev. B* **92**, 235103 (2015).
39. Das Sarma, S., Hwang, E. H. & Tse, W.-K. Many-body interaction effects in doped and undoped graphene: Fermi liquid versus non-Fermi liquid. *Phys. Rev. B* **75**, 121406 (2007).
40. Chang, P.-Y. & Coleman, P. Parity-violating hybridization in heavy Weyl semi-metals. *Phys. Rev. B* **97**, 155134 (2018).
41. Lai, H.-H., Grefe, S. E., Paschen, S. & Si, Q. Weyl–Kondo semimetal in heavy-fermion systems. *Proc. Natl Acad. Sci. USA* **115**, 93–97 (2018).
42. Guo, C. Y. et al. Evidence for Weyl fermions in a canonical heavy-fermion semimetal YbPtBi. *Nat. Commun.* **9**, 4622 (2018).
43. Shao, Y. et al. Electronic correlations in nodal-line semimetals. *Nat. Phys.* **16**, 636–641 (2020).
44. Qazilbash, M. M. et al. Electronic correlations in the iron pnictides. *Nat. Phys.* **5**, 647–650 (2009).
45. Degiorgi, L. Electronic correlations in iron-pnictide superconductors and beyond: lessons learned from optics. *N. J. Phys.* **13**, 023011 (2011).
46. Ma, J.-Z. et al. Spin fluctuation induced Weyl semimetal state in the paramagnetic phase of EuCd₂As₂. *Sci. Adv.* **5**, eaaw4718 (2019).
47. Destraz, D. et al. Magnetism and anomalous transport in the Weyl semimetal PrAlGe: possible route to axial gauge fields. *npj Quantum Mater.* **5**, 5 (2020).
48. Nagaosa, N., Sinova, J., Onoda, S., MacDonald, A. H. & Ong, N. P. Anomalous Hall effect. *Rev. Mod. Phys.* **82**, 1539–1592 (2010).
49. Weng, H., Yu, R., Hu, X., Dai, X. & Fang, Z. Quantum anomalous Hall effect and related topological electronic states. *Adv. Phys.* **64**, 227–282 (2015).
50. Corasaniti, M. et al. Electronic correlations in the van der Waals ferromagnet Fe₃GeTe₂ revealed by its charge dynamics. *Phys. Rev. B* **102**, 161109(R) (2020).
51. Dzsaber, S. et al. Giant spontaneous Hall effect in a nonmagnetic Weyl–Kondo semimetal. *Proc. Natl Acad. Sci. USA* https://www.pnas.org/content/118/8/e2013386118 (2021).
52. Fisk, Z. & Remeika, J. In *Handbook on the Physics and Chemistry of Rare Earths*, Vol. 12 Ch. 81 (Elsevier, 1989).
53. Kresse, G. & Hafner, J. Ab initio molecular dynamics for liquid metals. *Phys. Rev. B* **47**, 558(R)–561 (1993).
54. Kresse, G. & Furthmüller, J. Efficiency of ab-initio total energy calculations for metals and semiconductors using a plane-wave basis set. *Comp. Mater. Sci.* **6**, 15–50 (1996).
55. Kresse, G. & Furthmüller, J. Efficient iterative schemes for ab initio total-energy calculations using a plane-wave basis set. *Phys. Rev. B* **54**, 11169–11186 (1996).

AUTHOR CONTRIBUTIONS

L.D. and C.P. proposed and conceived the experiment. R.Y. and M.C. carried out the optical experiments while C.C.L. and C.Y. performed the first-principles calculations. Z.H. and C.P. supplied the specimen. Data analysis, figure planning and draft preparation was completed with input from all the authors. The project was supervised by L.D.

COMPETING INTERESTS

The authors declare no competing interests.

ADDITIONAL INFORMATION

Supplementary information The online version contains supplementary material available at https://doi.org/10.1038/s41535-022-00507-w.

Correspondence and requests for materials should be addressed to L. Degiorgi.

Reprints and permission information is available at http://www.nature.com/reprints

Publisher's note Springer Nature remains neutral with regard to jurisdictional claims in published maps and institutional affiliations.